

# Warm Molecular Gas in M51: Mapping the Excitation Temperature and Mass of H<sub>2</sub> with the Spitzer Infrared Spectrograph

Gregory Brunner<sup>1,2</sup>

*Department of Physics and Astronomy, Rice University,  
Houston, TX 77005*

`gbrunner@rice.edu`

Kartik Sheth<sup>3</sup>, Lee Armus<sup>3</sup>

*Spitzer Science Center, Caltech, Pasadena, CA 91125*

Mark Wolfire<sup>4</sup>, Stuart Vogel<sup>4</sup>

*Department of Astronomy, University of Maryland, College Park, MD 20741*

Eva Schinnerer<sup>5</sup>

*Max-Planck-Institut für Astronomie, Königstuhl 17, 69117 Heidelberg, Germany*

George Helou<sup>3</sup>

*Spitzer Science Center, Caltech, Pasadena, CA 91125*

Reginald Dufour<sup>1</sup>

*Department of Physics and Astronomy, Rice University, Houston, TX 77005*

John-David Smith<sup>6</sup>

*University of Arizona, Steward Observatory, Tucson, AZ 85721*

and

Daniel A. Dale<sup>7</sup>

*Department of Physics and Astronomy, University of Wyoming, Laramie, WY 82071*

## ABSTRACT

We have mapped the warm molecular gas traced by the  $\text{H}_2$  S(0) –  $\text{H}_2$  S(5) pure rotational mid-infrared emission lines over a radial strip across the nucleus and disk of M51 (NGC 5194) using the Infrared Spectrograph (IRS) on the *Spitzer Space Telescope*. The six  $\text{H}_2$  lines have markedly different emission distributions. We obtained the  $\text{H}_2$  temperature and surface density distributions by assuming a two temperature model: a warm ( $T = 100 - 300$  K) phase traced by the low  $J$  (S(0) – S(2)) lines and a hot phase ( $T = 400 - 1000$  K) traced by the high  $J$  (S(2) – S(5)) lines. The lowest molecular gas temperatures are found within the spiral arms ( $T \sim 155$  K), while the highest temperatures are found in the inter-arm regions ( $T > 700$  K). The warm gas surface density reaches a maximum of  $11 \text{ M}_\odot \text{ pc}^{-2}$  in the north-western spiral arm, whereas the hot gas surface density peaks at  $0.24 \text{ M}_\odot \text{ pc}^{-2}$  at the nucleus. The spatial offset between the peaks in the warm and hot phases and the differences in the distributions of the  $\text{H}_2$  line emission suggest that the warm phase is mostly produced by UV photons in star forming regions while the hot phase is mostly produced by shocks or X-rays associated with nuclear activity. The warm  $\text{H}_2$  is found in the dust lanes of M51, spatially offset from the brightest  $\text{H}\alpha$  regions. The warm  $\text{H}_2$  is generally spatially coincident with the cold molecular gas traced by CO ( $J = 1 - 0$ ) emission, consistent with excitation of the warm phase in dense photodissociation regions (PDRs). In contrast, the hot  $\text{H}_2$  is most prominent in the nuclear region. Here, over a  $0.5 \text{ kpc}$  radius around the nucleus of M51, the hot  $\text{H}_2$  coincides with  $[\text{O IV}](25.89 \text{ } \mu\text{m})$  and X-ray emission indicating that shocks and/or X-rays are responsible for exciting this phase.

*Subject headings:* galaxies: ISM — galaxies:  $\text{H}_2$  — galaxies: individual(M51)

---

<sup>1</sup>Department of Physics and Astronomy, Rice University, Houston, TX 77005

<sup>2</sup>Visiting Graduate Student Fellow, Spitzer Science Center, Caltech, Pasadena, CA 91125

<sup>3</sup>Spitzer Science Center, Caltech, Pasadena, CA 91125

<sup>4</sup>Department of Astronomy, University of Maryland, College Park, MD 20741

<sup>5</sup>Max-Planck-Institut für Astronomie, Königstuhl 17, 69117 Heidelberg, Germany

<sup>6</sup>University of Arizona, Steward Observatory, Tucson, AZ 85721

<sup>7</sup>Department of Physics and Astronomy, University of Wyoming, Laramie, WY 82071

## 1. Introduction

Star formation and galactic evolution are connected via the molecular gas in a galaxy. In the Milky Way, star formation occurs in molecular clouds, although not all clouds are actively forming stars. On a global, galactic scale, star formation may be triggered whenever the molecular gas surface density is enhanced, for example, by a spiral density wave (Vogel et al. 1988), by increased pressure or gas density in galactic nuclei (Young and Scoville 1991; Sakamoto et al. 1999; Sheth et al. 2005), by hydrodynamic shocks along the leading edge of bars (Sheth et al. 2000; Sheth et al. 2002), and in the transition region at the ends of bars (Kenny and Lord 1991; Sheth et al. 2002). How does this star formation affect the surrounding molecular gas? How is it heated and what is the distribution of the gas temperatures? How does the mass of the warm and hot gas vary from region to region? We address these questions using spectral line maps from a radial strip across the grand-design spiral galaxy, M51.

M51 (the Whirlpool galaxy, NGC 5194) is a nearby, face-on spiral galaxy that is rich in molecular gas. Its proximity (assumed to be 8.2 Mpc (Tully 1988)), face-on orientation, and grand-design spiral morphology make it the ideal target for studies of the interstellar medium (ISM) across distinct dynamical, chemical, and physical environments in a galaxy. Studies of the molecular gas within M51 have revealed giant molecular associations (GMAs) along the spiral arms (Vogel et al. 1988; Rand and Kulkarni 1990; Aalto et al. 1999), a reservoir of molecular gas in the nuclear region that is massive enough to fuel the active galactic nucleus (AGN) (Scoville et al. 1998), and spiral density wave triggered star-formation in molecular clouds (Vogel et al. 1988). In addition to being well-studied at millimeter and radio wavelengths, M51 has also been studied at X-ray, UV, optical, near-infrared, infrared, and submillimeter wavelengths (Palumbo et al. 1985; Terashima et al. 1998; Scoville et al. 2001; Calzetti et al. 2005; Matsushita et al. 2004; Meijerink et al. 2005).

In this paper we present maps of the  $\text{H}_2$  S(0) –  $\text{H}_2$  S(5) pure rotational mid-infrared lines over a strip across M51 created from *Spitzer Space Telescope* Infrared Spectrograph (IRS) spectral mapping mode observations. The mid-infrared  $\text{H}_2$  lines trace the warm ( $T = 100 - 1000$  K) phase of  $\text{H}_2$  and we use these lines to model the  $\text{H}_2$  excitation-temperature, mass (Rigopoulou et al. 2002; Higdon et al. 2006), and ortho-to-para ratio (Neufeld et al. 1998; Neufeld et al. 2006) across the M51 strips.<sup>1</sup> We use the inferred distributions to place constraints on the energy injection mechanisms (i.e. radiative heating, shocks, turbulence) that heat the warm molecular gas phase of the ISM.

---

<sup>1</sup>While we are always exploring the warm phase of  $\text{H}_2$ , in this paper we refer to a warm and a hot phase corresponding to temperatures of  $T = 100 - 300$  K and  $T = 400 - 1000$  K, respectively.

## 2. Observations and Data Reduction

### 2.1. Spectral Data

We mapped a radial strip across M51 using the short-low (SL;  $5 - 14.5 \mu\text{m}$ ) and long-low (LL;  $14 - 38 \mu\text{m}$ ) modules of the *Spitzer* IRS in spectral mapping mode (Houck et al. 2004). The radial strips were  $324'' \times 57''$  and  $295'' \times 51''$  in the SL and LL, respectively. Each slit position was mapped twice with half-slit spacings. In total, 1,412 spectra were taken in the SL and 100 were taken in the LL. Integration times for individual spectra were 14.6 s in both the SL and LL. Dedicated off-source background observations were taken for the SL observations. Backgrounds for the LL observations were taken from outrigger data collected while the spacecraft was mapping in the adjacent module. Figure 1 presents the astronomical observation requests (AORs) overlaid on the *Spitzer* Infrared Array Camera (IRAC)  $8 \mu\text{m}$  image of M51.

The spectra were assembled from the basic calibration data (BCD) into spectral data cubes for each module using CUBISM (Kennicutt et al. 2003; Smith et al. 2004; Smith et al. 2007a). Background subtraction and bad pixel removal were done within CUBISM. The individual BCDs were processed using the S14.0 version of the Spitzer Science Center (SSC) pipeline. In CUBISM, the SL and LL data cubes have  $1''.85$  and  $5''.08$  pixels, respectively. The pixel size is half the full width at half maximum (FWHM) of the point spread function (PSF) at the red end of a given module. In principle, the PSF should vary with wavelength but since the PSF is undersampled at the blue end of the module, it is approximately constant across a given module. So the approximate resolution of the SL and LL modules and maps of spectral features observed in the SL and LL modules is  $3''.7$  and  $10''.1$ , respectively.

We created continuum-subtracted line flux maps of the  $\text{H}_2 \text{ S}(0) - \text{H}_2 \text{ S}(5)$  lines using a combination of PAHFIT (Smith et al. 2007b) and our own code. PAHFIT is a spectral fitting routine that decomposes IRS low resolution spectra into broad PAH features, unresolved line emission, and grain continuum with the main advantage being that it allows one to recover the full line flux of any blended features. Several  $\text{H}_2$  lines are blended with PAH features and atomic lines in IRS low resolution spectra:  $\text{H}_2 \text{ S}(1)$  with the  $17.0 \mu\text{m}$  PAH complex,  $\text{H}_2 \text{ S}(2)$  with the  $12.0$  and  $12.6 \mu\text{m}$  PAH complexes,  $\text{H}_2 \text{ S}(4)$  with the  $7.8$  and  $8.6 \mu\text{m}$  PAH complexes, and  $\text{H}_2 \text{ S}(5)$  with the  $[\text{Ar II}](6.9 \mu\text{m})$  line. PAHFIT also solves for the foreground dust emission and dereddens the emitted line intensities. Our code concatenates SL1 and SL2, and LL1 and LL2 data cubes into two cubes, one for SL and one for LL and smoothes each map in the cubes by a  $3 \times 3$  pixel box, conserving the flux, to increase the signal-to-noise ratio of the spectra. Then, for each pixel, the spectrum is extracted and PAHFIT is run to decompose it. Our code saves the location of the pixel on the sky along with the

PAHFIT output (i.e. integrated line flux, line FWHM, line equivalent width, the uncertainty in the line flux, the fit to the entire spectrum and the fit to the continuum) for each spectrum and uses this information to construct line flux maps for all of the mid-infrared features. In addition to creating line maps, our code creates maps of line FWHM, line equivalent width, and uncertainty in the flux and data cubes of the fit to the entire spectrum, the fit to the continuum, a continuum-subtracted data cube, and a residual data cube. These parameters (the uncertainty in the line flux, line FWHM, and line equivalent width) are all determined within PAHFIT. For a more thorough discussion of how PAHFIT determines quantities such as the uncertainty in the integrated line flux, line FWHM, and line equivalent width, see Smith et al. (2007b).

Figure 2 presents sample *Spitzer* IRS low resolution spectra and the PAHFIT spectral decomposition for 3 different single pixel regions across the M51 strip. The SL and LL spectra are plotted separately because we decomposed the SL and LL data cubes separately. The locations of the regions are marked on the maps of the  $H_2$  surface density in Figure 5. While we have decomposed the entire spectrum and created maps of all of PAH features and spectral lines, in this paper we focus primarily on the  $H_2$  line maps.

## 2.2. Ancillary Data: CO ( $J = 1 - 0$ ), Optical $V$ Band, $H\alpha$ , and X-ray Observations

In this section we briefly discuss the ancillary data that we have used in order to understand  $H_2$  excitation in M51. We take note of the image resolutions for comparison to the *Spitzer* IRS beam. The Berkely Illinois Maryland Array (BIMA) CO ( $J = 1 - 0$ ) map was acquired as part of the BIMA Survey of Nearby Galaxies (SONG) (Regan et al. 2001; Helfer et al. 2003). At the distance of M51, the SONG beam ( $5''.8 \times 5''.1$ ) subtends  $220 \text{ pc} \times 190 \text{ pc}$ . The optical  $V$  band and continuum-subtracted  $H\alpha + [N \text{ II}]$  images of M51 were obtained from the *Spitzer Infrared Nearby Galaxies Survey* (SINGS) archive.<sup>2</sup> The native pixel scale for both images is  $0''.3$  and the angular resolutions are  $\sim 1''$ . X-ray emission from M51 was observed by the Advanced CCD Imaging Spectrometer (ACIS) on the *Chandra X-Ray Observatory* on 20 June 2000. The resolution of the image is  $\sim 1''$ . The X-ray image that we use has been presented and discussed in Terashima and Wilson (2001).

---

<sup>2</sup><http://data.spitzer.caltech.edu/popular/sings/>

### 3. Results

#### 3.1. The Distribution of H<sub>2</sub> Emission

We have detected and mapped H<sub>2</sub> emission from the six lowest pure rotational H<sub>2</sub> lines (Figure 3). The maps reveal remarkable differences in the distribution of H<sub>2</sub> emission in M51. H<sub>2</sub> S(0) emission is strongest in the northwest inner spiral arm peaking at a flux of  $3.7 \times 10^{-18} \text{ W m}^{-2}$  and decreases by a factor of 2 in the nuclear region. In contrast, the H<sub>2</sub> S(1) emission peaks in the nucleus of the galaxy at  $1.0 \times 10^{-17} \text{ W m}^{-2}$  and has an extension of equal brightness towards the northwest inner spiral arm. In the spiral arm itself, the H<sub>2</sub> S(0) peak is offset from the H<sub>2</sub> S(1) emission by  $10''$  ( $\sim 380 \text{ pc}$ ). We detect emission from the H<sub>2</sub> S(0) and H<sub>2</sub> S(1) lines to the outer limit of our radial strip,  $\sim 6 \text{ kpc}$  from the nucleus of the galaxy. In the outer spiral arms, the H<sub>2</sub> S(0) flux is a factor of 2 times lower than in the inner northwest spiral arm and the H<sub>2</sub> S(1) flux is a factor of 5 times lower than in the nucleus.

The H<sub>2</sub> S(2) – H<sub>2</sub> S(5) maps show different molecular gas distributions within M51 through each H<sub>2</sub> line. The brightest H<sub>2</sub> S(2) emission is from the nucleus at  $2.2 \times 10^{-18} \text{ W m}^{-2}$ . We also see bright H<sub>2</sub> S(2) emission from the inner northwest spiral arm at half the flux of the nuclear peak. The H<sub>2</sub> S(3) peak at the nucleus is  $1.4 \times 10^{-17} \text{ W m}^{-2}$ , a factor of  $\sim 6$  greater than the H<sub>2</sub> S(2) nuclear peak. There is also a linear bar-like structure in H<sub>2</sub> S(3) emission across the nucleus of the galaxy at a PA  $\sim -10^\circ$  and length of  $\sim 1.5 \text{ kpc}$ . The emission peaks in the H<sub>2</sub> S(2) and H<sub>2</sub> S(3) maps are not spatially coincident. For instance, in the northwest inner spiral arm the brightest H<sub>2</sub> S(3) emission is further down the spiral arm than the brightest H<sub>2</sub> S(2) emission. Offsets like these suggest variations in the excitation temperature from region to region within a galaxy, and even within a spiral arm.

The H<sub>2</sub> S(4) and H<sub>2</sub> S(5) lines are brightest at the nucleus with fluxes of 3.1 and  $8.0 \times 10^{-18} \text{ W m}^{-2}$ , respectively. The H<sub>2</sub> S(4) line shows emission in the nucleus and in the spiral arm to the west. In the spiral arm to the west of the nucleus, the H<sub>2</sub> S(4) flux is  $2.1 \times 10^{-18} \text{ W m}^{-2}$ . This is notable because the spiral arm to the southwest of the nucleus is very bright in CO and studies have revealed very high molecular gas column densities in the southwest inner spiral arm (Lord and Young 1990; Aalto et al. 1999). H<sub>2</sub> S(5) emission is asymmetric in the nucleus and mimics the morphology of the H<sub>2</sub> S(3) line with extended emission to the north of the nucleus. The trail of intensity peaks along the long northeast edge of the H<sub>2</sub> S(4) and H<sub>2</sub> S(5) maps is not real. It is likely due to difficulty smoothing the maps near the edges. These regions do not effect the determination of the H<sub>2</sub> temperature and surface density due to the offset of the SL strip relative to the LL strip.

Based on the uncertainty maps generated while creating the H<sub>2</sub> line maps, errors in the

H<sub>2</sub> S(0) line flux that range from 15% to 75% with the largest uncertainties being found in the inter-arm regions and the outer northwest and southeast spiral arms. Errors in the H<sub>2</sub> S(1) line fluxes range from 10% to 70% with the largest uncertainties being found at the distant northwest and southeast portions of the M51 strip. Errors in the H<sub>2</sub> S(2) and H<sub>2</sub> S(3) line fluxes range from 10% to 85% with the largest uncertainties being found toward the inter-arm regions. Errors in the H<sub>2</sub> S(4) and H<sub>2</sub> S(5) line fluxes are  $\sim 30\%$  and  $20\%$  within a 1 kpc radius of the nucleus and become higher moving radially away.

### 3.2. Mapping H<sub>2</sub> Excitation Temperature and Surface Density across M51

#### 3.2.1. Modeling H<sub>2</sub> Excitation Temperature and Surface Density

The pure rotational lines of molecular hydrogen provide a powerful probe of the conditions of the ISM by placing constraints on the energy injection that excites H<sub>2</sub>. For example, Neufeld et al. (2006) discuss shock excitation of H<sub>2</sub> and Kaufman et al. (2006) discuss H<sub>2</sub> excitation in photodissociation regions (PDRs). Using the maps of H<sub>2</sub> emission, we modeled the H<sub>2</sub> temperature and mass distribution over the radial strip in M51 following the methods described in Rigopoulou et al. (2002) and Higdon et al. (2006).

First, we smoothed the H<sub>2</sub> S(1) – H<sub>2</sub> S(5) maps to the resolution of the H<sub>2</sub> S(0) map,  $10''.1$ . The maps were then interpolated to the same spatial grid. Excitation diagrams across the strip were derived from the Boltzmann equation

$$N_i/N = (g(i)/Z(T_{\text{ex}}))\exp(-T_i/T_{\text{ex}}) \quad (1)$$

where  $g(i)$  is the statistical weight of state  $i$ ,  $Z(T_{\text{ex}})$  is the partition function,  $T_i$  is the energy level of a given state, and  $T_{\text{ex}}$  is the excitation temperature.  $N$  and  $N_i$  are the total column density and the column density of a given state  $i$  and  $N_i$  is determined directly from the measured extinction-corrected flux by

$$N_i = 4\pi \times \text{flux}(i)/(\Omega A(i)h\nu(i)) \quad (2)$$

where  $A(i)$  is the Einstein  $A$ -coefficient,  $\nu(i)$  is the frequency of state  $i$ ,  $\Omega$  is the solid angle of the beam, and  $h$  is Planck's constant. Table 1 lists the values for the wavelength, rotational state, Einstein  $A$ -coefficient, energy, and statistical weight of the pure rotational levels of H<sub>2</sub>.

In order to derive temperature and surface density distributions we assume a two temperature model for the H<sub>2</sub>. To determine the hot ( $T = 400 - 1000$  K) phase temperature, we do a least squares fit to the H<sub>2</sub> S(2) – H<sub>2</sub> S(5) column densities in the excitation diagram

at every pixel in our maps. We then subtract the contribution of the hot phase from the lower  $J$  lines and do a least squares fit to the column densities of  $\text{H}_2 \text{ S}(0) - \text{H}_2 \text{ S}(2)$  lines at every pixel in our maps to determine the temperature distribution of the warm ( $T = 100 - 300 \text{ K}$ ) phase. The warm and hot phase surface density distributions are derived from the column densities of the  $\text{H}_2 \text{ S}(0)$  and  $\text{H}_2 \text{ S}(3)$  lines, respectively. The column densities are easily converted to mass surface density by determining the mass of the warm and hot  $\text{H}_2$  within every pixel.

Figure 4 shows excitation diagrams and the fits to the warm and hot  $\text{H}_2$  phases for three different regions across the M51 strip. The three regions are marked on the  $\text{H}_2$  surface density maps in Figure 5. In the nuclear region (Region 2) the ortho and para levels appear to lie along the same curve indicating an ortho-to-para ratio (OPR) of 3; the excitation diagrams do not exhibit the “zigzag” characteristic of a non-equilibrium  $\text{H}_2$  OPR (Neufeld et al. 1998; Fuente et al. 1999). The slope of the curve appears to decrease as the rotational state increases indicating that we are sampling a continuous range of  $\text{H}_2$  temperatures with the higher rotational states ( $\text{S}(2) - \text{S}(5)$ ) probing a hotter phase of  $\text{H}_2$  than the lower rotational states ( $\text{S}(0) - \text{S}(2)$ ). In the southeast and northwest spiral arms (Regions 1 and 3, respectively) the lower  $J$  ( $\text{H}_2 \text{ S}(0) - \text{H}_2 \text{ S}(3)$ ) levels exhibit an OPR of  $\sim 3$ . The  $\text{H}_2 \text{ S}(4)$  measurement shows significant scatter in the excitation diagrams outside of the nuclear region of M51. This would indicate that the OPR is less than 3, however, due to the low signal-to-noise ratio of the  $\text{H}_2 \text{ S}(4)$  map, we do not believe that the OPR determined from the  $\text{H}_2 \text{ S}(4)$  flux reflects the OPR of the warm  $\text{H}_2$ . We assume an OPR of 3 when deriving the  $\text{H}_2$  temperature and mass distributions, which is consistent with Roussel et al. (2007) who found an OPR of 3 for the nuclear region and four of seven HII regions studied in M51.

### 3.2.2. Warm and Hot $\text{H}_2$ Excitation Temperature and Surface Density Distributions

Figure 5 presents the warm (*left*) and hot (*right*)  $\text{H}_2$  surface density distributions across the M51 strip.<sup>3</sup> The highest gas surface density for the warm  $\text{H}_2$  phase is in the inner northwest spiral arm at  $11 \text{ M}_\odot \text{ pc}^{-2}$ . The gas surface density in the outer northwest and southeast spiral arms is maximum at the center of the spiral arms at  $3.5 \text{ M}_\odot \text{ pc}^{-2}$  and  $1.0 \text{ M}_\odot \text{ pc}^{-2}$  respectively. The hot phase surface density is highest in the nucleus and interior to the inner spiral arm at  $0.24 \text{ M}_\odot \text{ pc}^{-2}$ . The gas surface density of the hot phase in the spiral arms is 3 – 5 times lower than that of the nuclear region.

Figures 6 and 7 show the distribution of the warm and hot  $\text{H}_2$  temperatures (in grayscale)

---

<sup>3</sup>Note that the non-rectangular shape of the strip is due to the offset between the SL and LL strips.



with the contours of the warm and hot  $\text{H}_2$  surface densities overlaid, respectively. In both cases we see that the temperature and surface density are inversely correlated with the hottest temperatures corresponding to regions of lowest surface density. For both the warm and hot phases, we see the temperature is higher in the inter-arm regions than in the spiral arms. This is real and does not result from lower signal-to-noise in the inter-arm regions. We tested this by extracting spectra over  $0.76 \text{ kpc}^2$  inter-arm regions between the northwest inner arm and northwest arm and between the southeast inner arm and southeast arm and found warm  $\text{H}_2$  temperatures of 177 and 175 K and hot  $\text{H}_2$  temperatures of 691 and 690 K, respectively. These temperatures are higher than the 150 - 165 K warm  $\text{H}_2$  temperatures and the 550 - 650 K hot  $\text{H}_2$  temperatures found in the spiral arms.

Figure 8 compares the warm (in grayscale) and hot (in contours)  $\text{H}_2$  surface density distributions. The warm  $\text{H}_2$  mass distribution peaks in the northwest inner spiral arm and the hot  $\text{H}_2$  mass distribution peaks in the nucleus and in the region interior to the northwest spiral arm. The warm-to-hot  $\text{H}_2$  mass ratio is not constant across the galaxy but is lowest ( $\sim 12$ ) in the nucleus of the galaxy and increases to 170 and 136 in the southeast and northwest spiral arms, respectively.

## 4. Discussion

### 4.1. Effects of Beam Averaging on Studies of Extragalactic $\text{H}_2$

Previous studies have used aperture-averages over entire galactic nuclei to derive the physical conditions of the molecular gas (Rigopoulou et al. 2002; Higdon et al. 2006; Roussel et al. 2007). In M51, Roussel et al. (2007) find that within the central  $330 \text{ arcsec}^2$  ( $4.61 \times 10^5 \text{ pc}^2$ ), the warm  $\text{H}_2$  phase has a temperature of 180 K and a surface density of  $3.2 \text{ M}_\odot \text{ pc}^{-2}$  (a total mass of  $M_{\text{warm}} = 1.5 \times 10^6 \text{ M}_\odot$ ). Roussel et al. (2007) have also measured the temperature of the hot phase (though they do not measure the mass in the hot phase) and find a hot  $\text{H}_2$  temperature of 521 K.

Having spatially resolved spectra over a strip across M51, we can investigate the behavior of the warm and hot  $\text{H}_2$  phases on smaller scales. In the nuclear region of M51 we see that the warm phase temperature peaks at 192 K and decreases radially towards the inner spiral arms. The warm  $\text{H}_2$  surface density at the nucleus is  $4.4 \text{ M}_\odot \text{ pc}^{-2}$  and decreases over a  $0.5 \text{ kpc}$  radius surrounding the nucleus. To check the consistency of our results against those of Roussel et al. (2007), we averaged the warm phase temperature over a similar  $412 \text{ arcsec}^2$  ( $5.76 \times 10^2 \text{ pc}^2$ ) aperture and found that the warm phase temperature and surface density are 186 K and  $2.8 \text{ M}_\odot \text{ pc}^{-2}$ , respectively. Our results are consistent with previous studies

of warm  $\text{H}_2$  done at lower resolution and suggest that previous studies of the warm  $\text{H}_2$  temperature and mass have yielded average values rather than a maximum (or minimum) values.

## 4.2. Distinguishing the $\text{H}_2$ Excitation Mechanisms

The warm-to-hot  $\text{H}_2$  surface density ratio varies across M51 suggesting that the  $\text{H}_2$  excitation mechanisms have different effects on the warm and hot phases. The largest warm  $\text{H}_2$  surface densities are found in the spiral arms suggesting that the warm phase is associated with star formation activity. The largest hot  $\text{H}_2$  surface densities are found in the nuclear region of M51. This suggests that where nuclear activity is the dominant excitation mechanism, a larger fraction of the  $\text{H}_2$  can be maintained in the hot phase and that  $\text{H}_2$  is generally more efficiently heated by nuclear activity. This is further supported by the fact that the hot  $\text{H}_2$  surface density is  $\sim 660$  K in the nuclear region and decreases to  $\sim 530$  K and 550 K in the inner northwest and southeast spiral arms, respectively. Roussel et al. (2007) find that  $\text{H}_2$  is generally heated by massive stars in PDRs, however, Seyferts and LINERs show evidence for the dominance of other excitation mechanisms such as X-rays or shocks. By comparing the spatial distribution of the warm and hot  $\text{H}_2$  to optical  $V$  band imagery,  $\text{H}\alpha$ , and  $\text{CO}$  ( $J = 1 - 0$ ) emission, we can investigate the relationship between star formation and  $\text{H}_2$ . Additionally, by comparing the warm and hot  $\text{H}_2$  distributions to X-ray observations and the spatial distribution of  $[\text{O IV}](25.89 \mu\text{m})$  emission, we can investigate X-ray and shock heating of  $\text{H}_2$  within M51.

Kaufman et al. (2006) show that within galaxies, where the telescope beam size is generally kiloparsecs across,  $\text{H}_2$  emission could serve to probe the average physical conditions in the surfaces of molecular clouds. In Figure 9, we compare the warm (*left*) and hot  $\text{H}_2$  (*right*) mass distributions to the cold molecular gas traced by  $\text{CO}$  ( $J = 1 - 0$ ) emission. The warm and hot  $\text{H}_2$  phases appear to trace the bright  $\text{CO}$  emission in the northwest and southeast spiral arms. Comparison of  $\text{CO}$  to the individual  $\text{H}_2$   $\text{S}(0) - \text{H}_2$   $\text{S}(3)$  line intensity maps in Figure 10 also shows that the  $\text{H}_2$  in the spiral arms traces the bright  $\text{CO}$  emission. In the spiral arms, both the warm and hot  $\text{H}_2$  phases are found in PDRs and are associated with star formation activity. The most striking result is that in the inner spiral arms, we see that the  $\text{CO}$  is offset toward the nucleus from the warm  $\text{H}_2$  mass (in Figure 9). The offset between the peaks in  $\text{CO}$  and warm  $\text{H}_2$  mass is  $7''$  in the northwest inner spiral arm and  $5''$  in the southeast inner spiral arm. We believe that these offsets are real with one possible explanation being that the  $\text{H}_2$  is tracing the regions of active star-formation within the giant molecular associations.

In Figures 11 and 12, we compare the warm (*left*) and hot (*right*)  $\text{H}_2$  mass distributions to  $\text{H}\alpha$  emission and an optical  $V$  band image, respectively. The  $\text{H}\alpha$  image reveals the brightest HII regions and the  $V$  band image shows the dust lanes in M51. In general, the warm and hot  $\text{H}_2$  concentrations are not cospatial with the brightest  $\text{H}\alpha$  emission regions in the spiral arms with the one exception being that the warm  $\text{H}_2$  mass in the northwest and southeast inner spiral arms appears to trace the  $\text{H}\alpha$  emission. The warm  $\text{H}_2$  mass contours show that local peaks in  $\text{H}_2$  mass are found within the dust lanes, with the  $\text{H}\alpha$  emission spatially offset towards the leading edge of the spiral arms. An example of this is in the northwest spiral arms where we see the  $\text{H}_2$  mass offset from the  $\text{H}\alpha$  spiral arms with local peaks being found in the dust lanes. In Figures 13 and 14, we compare the  $\text{H}_2$  S(0) –  $\text{H}_2$  S(3) line intensity maps to  $\text{H}\alpha$  emission and  $V$  band imagery, respectively. Comparison of the  $\text{H}_2$  S(0) map to  $\text{H}\alpha$  reveals that the strongest  $\text{H}_2$  emission in the northwest and southeast inner spiral arms is coincident with  $\text{H}\alpha$  emission; however, the other  $\text{H}_2$  S(0) spiral arms show the strongest emission in the dust lanes, offset from the  $\text{H}\alpha$  spiral arms. The largest offsets are seen in the southeast spiral arm where the  $\text{H}_2$  S(0) emission is offset from the  $\text{H}\alpha$  spiral arm by  $\sim 15''$  (560 pc).  $\text{H}_2$  S(1) emission appears to follow the dust lanes and the  $\text{H}_2$  S(1) intensity subsides into the  $\text{H}\alpha$  spiral arms.  $\text{H}_2$  S(2) and  $\text{H}_2$  S(3) emission is also found in the dust lanes; however, there are instances (such as in the southeast spiral arm) where the  $\text{H}_2$  emission appears to be found straddling the dust lane and  $\text{H}\alpha$  spiral arm.

The  $[\text{O IV}](25.89 \mu\text{m})$  line can be excited in fast shocks ( $v_s > 100 \text{ km s}^{-1}$ ) (Lutz et al. 1998), by photoionization in Wolf-Rayet stars (Schaerer and Stasinska 1999), or by an AGN (Smith et al. 2004). We have mapped the blended  $[\text{O IV}](25.89 \mu\text{m}) + [\text{Fe II}](25.99 \mu\text{m})$  line across M51. While the map contains the contribution of both lines, we have examined the SINGS high resolution spectra and find that averaged over a  $365 \text{ arcsec}^2$  region around the nucleus of M51, the  $[\text{O IV}]$  line flux is 2.7 times higher than the  $[\text{Fe II}]$  flux.<sup>4</sup> In the high resolution data cubes of the nuclear region, the  $[\text{O IV}]$  line flux dominates the  $[\text{O IV}] + [\text{Fe II}]$  blend and the  $[\text{O IV}]$  emission distribution derived from the low resolution spectra accurately reflects the distribution seen in the high resolution spectra. In Figure 15, we compare the  $[\text{O IV}]$  surface brightness to the warm (*left*) and hot (*right*)  $\text{H}_2$  distributions. The  $[\text{O IV}]$  emission is brightest in the nuclear region at  $1.2 \times 10^{-17} \text{ W m}^{-2}$  and within a 0.5 kpc radius of the nucleus, the peak is coincident with the peak in the mass of the hot  $\text{H}_2$ .  $[\text{O IV}]$  surface brightness decreases from the nucleus to the inner spiral arm by 50 %. We resolve weaker  $[\text{O IV}]$  emission within the warm and hot  $\text{H}_2$  spiral arms. The  $[\text{O IV}]$  surface brightness is a factor of  $\sim 6$  lower in the spiral arms than the peak intensity found in the nucleus. The  $[\text{O IV}]$  emission within the nuclear region of M51 is likely due to the weak Seyfert 2 nucleus

---

<sup>4</sup>SINGS data cubes and spectra for M51 can be found at <http://irsa.ipac.caltech.edu/data/SPITZER/SINGS/galaxies/ngc/>

(Ford et al. 1985) and is possibly associated with shocked gas from the outflows of the AGN. The peak of the [O IV] emission coincides with the nuclear peak in hot H<sub>2</sub> mass, indicating that the hot H<sub>2</sub> phase in the nuclear region of the galaxy is AGN or shock heated. In the nuclear region we observe a factor of 12 times greater warm H<sub>2</sub> mass than the hot H<sub>2</sub> mass. The warm H<sub>2</sub> mass is much greater within the spiral arms than within the nucleus and the warm-to-hot mass ratio is lowest in the nuclear region where the [O IV] flux is greatest. In general, nuclear activity and shocks heat the ISM more efficiently causing the higher surface density of hot H<sub>2</sub>.

X-ray studies of M51 have revealed bright X-ray emission from the nucleus, the extranuclear cloud (XNC, to the south of the nucleus), and the northern loop (Terashima and Wilson 2001; Maddox et al. 2007). A radio jet that is believed to be shock heating the ISM has been observed emanating from the south of the nucleus towards the XNC in 6 cm imagery (Crane and van der Hulst 1992). In Figure 16, we compare the smoothed 0.5 - 10 keV band X-ray image to the warm (*left*) and hot (*right*) H<sub>2</sub> mass distributions. The 0.5 - 10 keV band has been smoothed to the resolution of the warm and hot H<sub>2</sub> mass distributions and the nucleus, XNC, and northern loop are indistinguishable in the smoothed image. X-ray emission is brightest in the nucleus and decreases into the northwest spiral arm that contains the greatest H<sub>2</sub> mass. There appears to be very little connection between the 0.5 - 10 keV X-ray band and the warm H<sub>2</sub> mass distribution. The peak in X-ray emission is coincident with the hot H<sub>2</sub> mass peak. The brightest 0.5 - 10 keV X-ray emission originates from the nucleus and is oriented north-to-south, similar to the [O IV](25.89  $\mu$ m) emission. The peak in X-ray emission is located within the peak in hot H<sub>2</sub> mass suggesting that X-rays play an important role in producing the hot H<sub>2</sub> phase. While there is a correlation between X-ray emission and the hot H<sub>2</sub> phase, H<sub>2</sub> excitation by X-rays cannot be distinguished from H<sub>2</sub> excitation by shocks. In Figure 17, we compare the X-ray surface brightness to the H<sub>2</sub> S(2) – H<sub>2</sub> S(5) maps and find that the nuclear H<sub>2</sub> emission appears to be correlated with the X-ray source.

## 5. Conclusions

We have spectrally mapped a strip across M51 using the *Spitzer* IRS low resolution modules. We used the spatially resolved spectra to map H<sub>2</sub> S(0) – H<sub>2</sub> S(5) lines across the strip. We find:

1. The distribution of H<sub>2</sub> emission in M51 varies with H<sub>2</sub> rotational level. H<sub>2</sub> S(0) emission is brightest in the spiral arms of the galaxy while the higher  $J$  transitions show the strongest

emission towards the nucleus. The  $\text{H}_2$  S(1) line is brightest in the nuclear region and is offset from the peak in  $\text{H}_2$  S(0) intensity in the inner northwest spiral arm by  $10''$ . The  $\text{H}_2$  S(2) and  $\text{H}_2$  S(3) maps show  $\text{H}_2$  emission in the nucleus, spiral arms, and inter-arm regions of M51 and bar structure aligned north-to-south is apparent in  $\text{H}_2$  S(3) emission.  $\text{H}_2$  S(4) and  $\text{H}_2$  S(5) emission is resolved in the nuclear region of M51.

2. The different distributions of  $\text{H}_2$  emission in M51 indicate significant spatial variations in  $\text{H}_2$  temperature and surface density. Using the low  $J$  (S(0) – S(2)) lines to trace the warm ( $T = 100 - 300$  K)  $\text{H}_2$ , we find that the warm  $\text{H}_2$  temperature is highest in the nuclear region at 192 K and the warm  $\text{H}_2$  surface density peaks in the northwest inner spiral arm at  $11 \text{ M}_\odot \text{ pc}^{-2}$ . Using the higher  $J$  (S(2) – S(5)) lines to trace the hot ( $T = 400 - 1000$  K)  $\text{H}_2$ , we find that the hot  $\text{H}_2$  temperature is lowest in the inner spiral arms ( $500 - 550$  K) and increases to  $\sim 600$  K in the nucleus where the largest hot  $\text{H}_2$  surface density is found to be  $0.24 \text{ M}_\odot \text{ pc}^{-2}$ .

3. The warm and the hot  $\text{H}_2$  surface density distributions are not cospatial and the warm-to-hot surface density ratio varies across M51. The warm  $\text{H}_2$  surface density distribution peaks in the northwest spiral arm and is offset from the hot mass peak by  $11''$ . The hot  $\text{H}_2$  surface density distribution shows two peaks, one in the nucleus of M51 and one located interior to the northwest inner spiral arm of M51. Variations in the warm-to-hot  $\text{H}_2$  ratio and differences in the distributions of the  $\text{H}_2$  line emission across M51 suggest that the warm  $\text{H}_2$  is mostly produced by UV photons in star forming regions while the hot  $\text{H}_2$  is mostly produced by shocks or X-rays associated with nuclear activity.

4. The warm  $\text{H}_2$  follows the cold molecular gas traced by CO in the spiral arms of M51 indicating that the warm phase is associated with the surface layers of dense molecular clouds. The  $\text{H}_2$  S(0) –  $\text{H}_2$  S(3) contours trace the CO; however, within the spiral arms, the peaks in  $\text{H}_2$  can be offset from the peaks in CO intensity.

5. Comparing the distributions of  $\text{H}_2$  to  $V$  band imagery and  $\text{H}\alpha$  emission reveals that the warm and hot  $\text{H}_2$  in the spiral arms is found in the dust lanes rather than spatially coincident with the  $\text{H}\alpha$  emission.

6. [O IV]( $25.89 \mu\text{m}$ ) emission and X-ray intensity peak in the nuclear region of M51 and their peaks are spatially coincident with the peak in hot  $\text{H}_2$  surface density. This implies that the hot  $\text{H}_2$  is more efficiently heated by the AGN, shocks (possibly associated with the AGN), or X-rays associated with the AGN. The spatial distributions of the [O IV] emission and X-ray surface brightness are very similar preventing the characterization of the primary excitation mechanism (shocks or X-rays) of the hot  $\text{H}_2$  phase in the nuclear region.

The author graciously acknowledges the Spitzer Science Center Spitzer Visiting Graduate Student Fellowship program and committee for providing support for this research. The author would like to specifically acknowledge the program coordinators, Phil Appleton and Alberto Noriega-Crepso. The authors would also like to thank the anonymous referee who helped to clarify our results and improve our discussion. Partial support for the completion and preparation for publication of this study by the author was provided by AURA grant GO10822.1 to Rice University.

*Facilities:* Spitzer Science Center (SSC), Spitzer Space Telescope (SST), Berkely-Illinois-Maryland Array (BIMA).

## REFERENCES

- Aalto, S., Huttemeister, S., Scoville, N.Z., and Thaddeus, P., 1999, *AJ*, 522, 165
- Calzetti, D. et al., 2005, *ApJ*, 633, 871
- Crane, P.C. and van der Hulst, J.M., 1992, *AJ*, 103, 1146
- Ford, H.C., Crane, P.C., Jacoby, G.H., Lawrie, D.G., and van der Hulst, J.M., 1985, *ApJ*, 293, 132
- Fuente, A., Martín-Pintado, J., Rodríguez-Fernández, N.J., Rodríguez-Franco, A., de Vicente, P., and Kunze, D., 1999, *ApJ*, 518, L45
- Helfer, T.T., Thornley, M.D., Regan, M.W., Wong, T., Sheth, K., Vogel, S.N., Blitz, L., and Bock, D.C.J., 2003, *ApJS*, 145, 259
- Higdon, S.J.U., Armus, L., Higdon, J.L., Soifer, B.T., and Spoon, H.W.W., 2006, *ApJ*, 648, 323
- Houck, J.R. et al., 2004, *ApJS*, 145, 18
- Kaufman, M.J., Wolfire, M.G., and Hollenbach, D.J., 2006, *ApJ*, 644, 283
- Lord, S.D. and Young, J.S., 1990, *ApJ*, 356, 135
- Lutz, D., Kunze, D., Spoon, H.W.W., and Thornley, M.D., 1998, *A&A*, 333, L75

- Kennicutt, R.C. et al., 2003, PASP, 115, 928
- Kenny, J.D.P. and Lord, S.D., 1991, ApJ, 381, 118
- Maddox, L.A., Cowan, J.J., Kilgard, R.E., Schinnerer, E., and Stockdale, C.J., 2007, AJ, 133, 2559
- Matsushita, S. et al., 2004, ApJ, 616, L55
- Meijerink, R., Tilanus, R.P.I., Dullemond, C.P., Israel, F.P., and van der Werf, P.P., 2005, A&A, 430, 427
- Neufeld, D.A., Melnick, G.J., and Harwit, M., 1998, ApJ, 506, L75
- Neufeld, D.A., Melnick, G.J., Sonnentrucker, P., Bergin, E.A., Green, J.D., Kim, K.H., Watson, D.M., Forrest, W.J., and Pipher, J.L., 2006, ApJ, 649, 816
- Palumbo, G.G.C., Fabbiano, G., Fransson, C., and Trinchieri, G., 1985, ApJ, 298, 259
- Rand, R.J. and Kulkarni, S.R., 1990, ApJ, 349, L43
- Regan, M.W., Thornley, M.D., Helfer, T.T., Sheth, K., Wong, T., Vogel, S.N., Blitz, L., and Bock, D.C.J., 2001, ApJ, 561, 218
- Rigopoulou, D., Kunze, D., Lutz, D., Genzel, R., and Moorwood, A.F.M., 2002, A&A, 389, 374
- Roussel, H. et al., 2007, ApJS, in press
- Sakamoto, K., Okumura, S.K., Ishizuki, S., and Scoville, N.Z., 1999, ApJ, 525, 691
- Schaerer, D. and Stasinska, G., 1999, A&A, 345, L17
- Scoville, N.Z., Yun, M.S., Armus, L., and Ford, H., 1998, ApJ, 493, L63
- Scoville, N.Z., Polletta, M., Ewald, S., Stolovy, S.R., Thompson, R., and Rieke, M., 2001, AJ, 122, 3017
- Sheth, K., Regan, M.W., Vogel, S.N., and Teuben, P.J., 2000, ApJ, 532, 221
- Sheth, K., Vogel, S.N., Regan, M.W., Teuben, P.J., Harris, A.I., and Thornley, M.D., 2002, AJ, 124, 2581
- Sheth, K., Vogel, S.N., Regan, M.W., Thornley, M.D., and Teuben, P.J., 2005, ApJ, 632, 217

- Smith, J.D.T. et al., 2004, ApJS, 154, 199
- Smith, J.D.T. et al., 2007a, PASP, submitted
- Smith, J.D.T. et al., 2007b, ApJ, 656, 770
- Terashima, Y., Ptak, A., Fujimoto, M.I., Kunieda, H., Makishima, K., and Sherlemitsos, P.J., 1998, ApJ, 496, 210
- Terashima, Y. and Wilson, A.S., 2001, ApJ, 560, 139
- Tully, R.B. 1988, Nearby Galaxies Catalog (Cambridge: Cambridge University Press)
- Vogel, S.N., Kulkarni, S.R., and Scoville, S.Z., 1988, Nature, 334, 402
- Young, J.S. and Scoville, N.Z., 1991, ARA&A, 29, 581



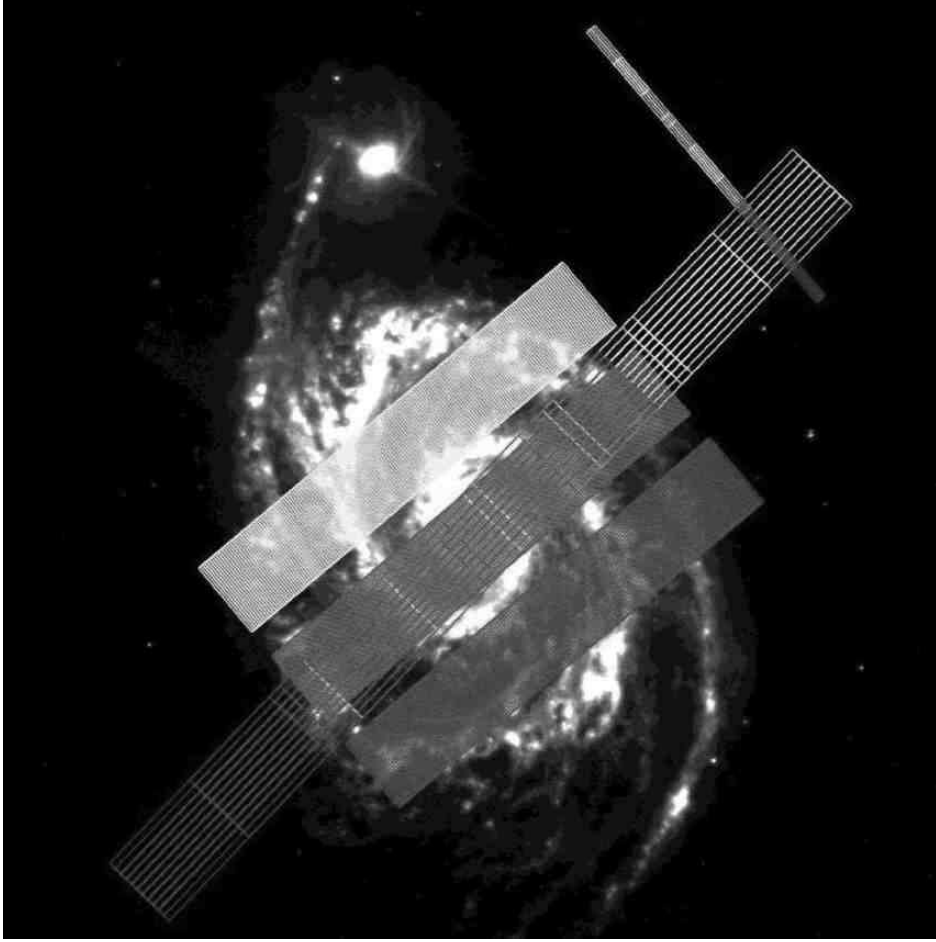


Fig. 1.— Overlay of the IRS footprints on the *Spitzer* IRAC  $8\,\mu\text{m}$  image of M51. The three parallel strips mark the SL ( $5 - 14.5\,\mu\text{m}$ ) observations with the white strip denoting the SL2 ( $5 - 7.5\,\mu\text{m}$ ) coverage and the grey strip denoting the SL1 ( $7.5 - 14.5\,\mu\text{m}$ ) coverage. The central strip is where the SL1 and SL2 overlap along with the LL ( $14 - 38\,\mu\text{m}$ ) radial strip giving us complete coverage of the mid-infrared spectrum across the nucleus and disk of M51. The small off-galaxy strip is the SL background observation.

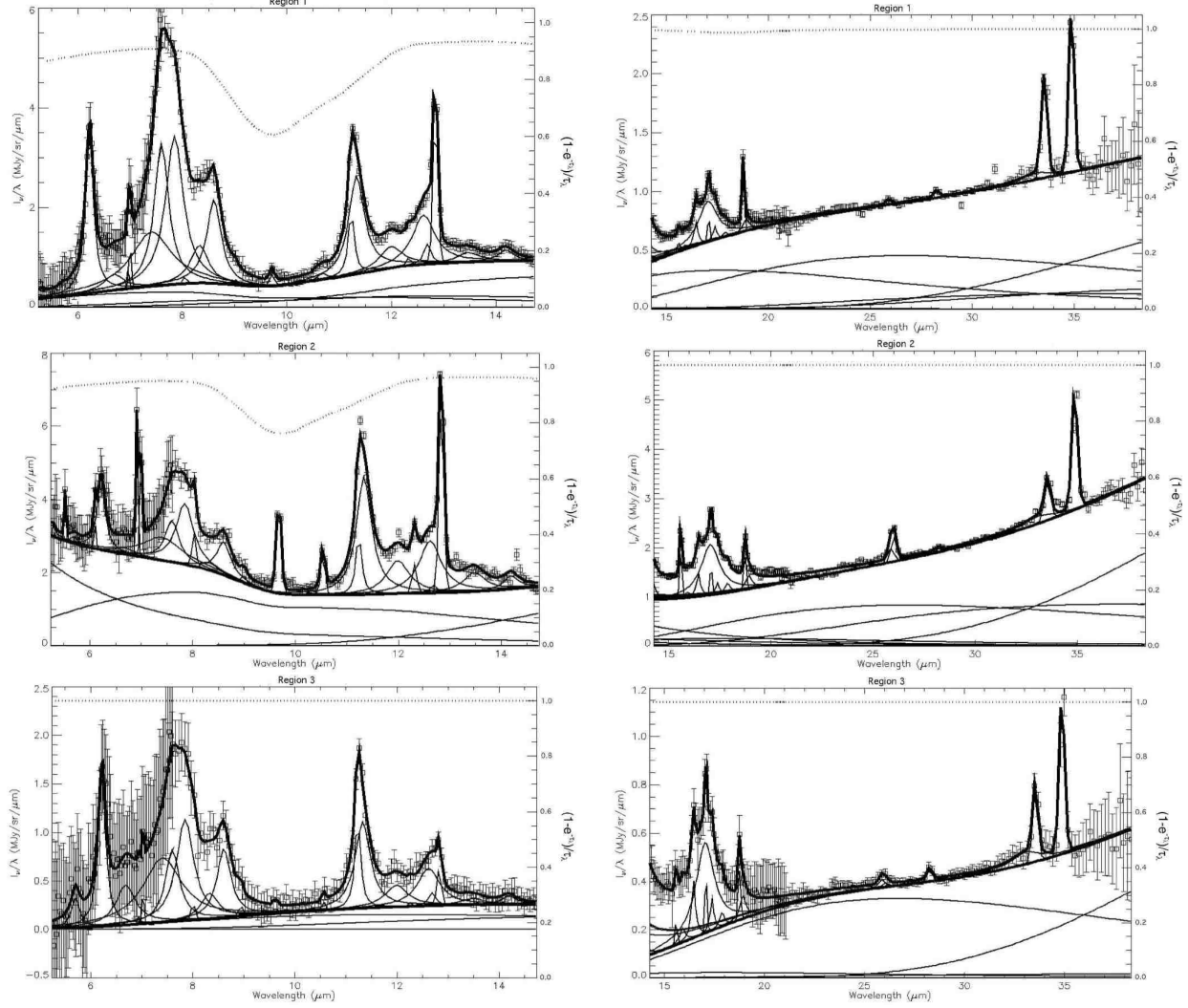


Fig. 2.— Shown are sample *Spitzer* IRS low resolution spectra and the PAHFIT spectral decomposition for 3 different single pixel regions across the M51 strip. The SL and LL spectra are plotted separately because we decomposed the SL and LL data cubes separately. The locations of the regions are marked on the maps of the  $H_2$  surface density in Figure 5.

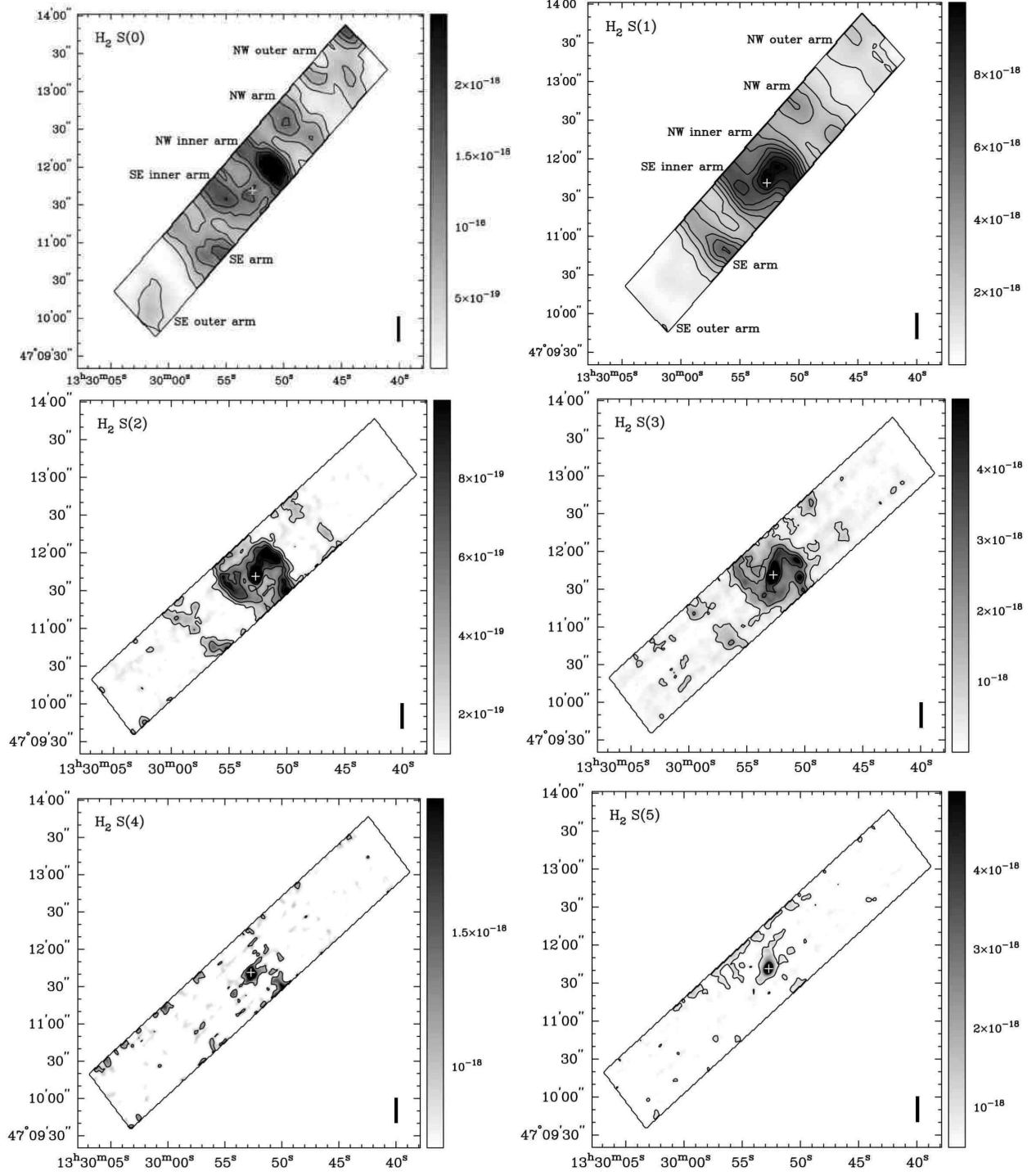


Fig. 3.— Maps of the H<sub>2</sub> S(0) (*top left*), H<sub>2</sub> S(1) (*top right*), H<sub>2</sub> S(2) (*middle left*), H<sub>2</sub> S(3) (*middle right*), H<sub>2</sub> S(4) (*bottom left*), and H<sub>2</sub> S(5) (*bottom right*) line fluxes across the SL and LL strips that we mapped with the *Spitzer* IRS. The H<sub>2</sub> S(0) and H<sub>2</sub> S(1) maps are created from the LL data cube. The H<sub>2</sub> S(2), H<sub>2</sub> S(3), H<sub>2</sub> S(4), and H<sub>2</sub> S(5) maps are created from the SL data cube. The grayscale is in units of W m<sup>-2</sup>. Contour levels are at  $3.7 \times 10^{-19}$ ,  $7.3 \times 10^{-19}$ ,  $1.1 \times 10^{-18}$ ,  $1.5 \times 10^{-18}$ ,  $1.8 \times 10^{-18}$ ,  $2.2 \times 10^{-18}$ , and  $2.9 \times 10^{-18}$  W m<sup>-2</sup> for H<sub>2</sub> S(0);  $1.1 \times 10^{-18}$ ,  $2.1 \times 10^{-18}$ ,  $3.2 \times 10^{-18}$ ,  $4.3 \times 10^{-18}$ ,  $5.4 \times 10^{-18}$ ,  $6.4 \times 10^{-18}$ ,  $7.5 \times 10^{-18}$ ,  $8.6 \times 10^{-18}$ , and  $9.6 \times 10^{-18}$  W m<sup>-2</sup> for H<sub>2</sub> S(1);  $2.2 \times 10^{-19}$ ,  $4.4 \times 10^{-19}$ ,  $6.7 \times 10^{-19}$ ,  $8.9 \times 10^{-19}$ , and  $1.1 \times 10^{-18}$  W m<sup>-2</sup> for H<sub>2</sub> S(2);  $1.3 \times 10^{-18}$ ,  $4.0 \times 10^{-18}$ ,  $6.7 \times 10^{-18}$ ,  $9.4 \times 10^{-18}$ , and  $1.2 \times 10^{-17}$  W m<sup>-2</sup> for H<sub>2</sub> S(3);  $1.0 \times 10^{-18}$  and  $2.0 \times 10^{-18}$  W m<sup>-2</sup> for H<sub>2</sub> S(4);  $8.0 \times 10^{-19}$ ,  $4.0 \times 10^{-18}$ , and  $7.3 \times 10^{-18}$  W m<sup>-2</sup> for H<sub>2</sub> S(5). The vertical axis is the right ascension and the horizontal axis is the declination. In all of the maps, north is up, east is to the left, and the cross denotes the nucleus of the galaxy. The different spiral arm regions are labeled on the H<sub>2</sub> S(0) and H<sub>2</sub> S(1) maps in order to aid in discussing the molecular gas morphologies. The bar in the bottom right corner of the maps represents 1 kiloparsec. The box around the maps represents the SL or LL strip that we mapped.

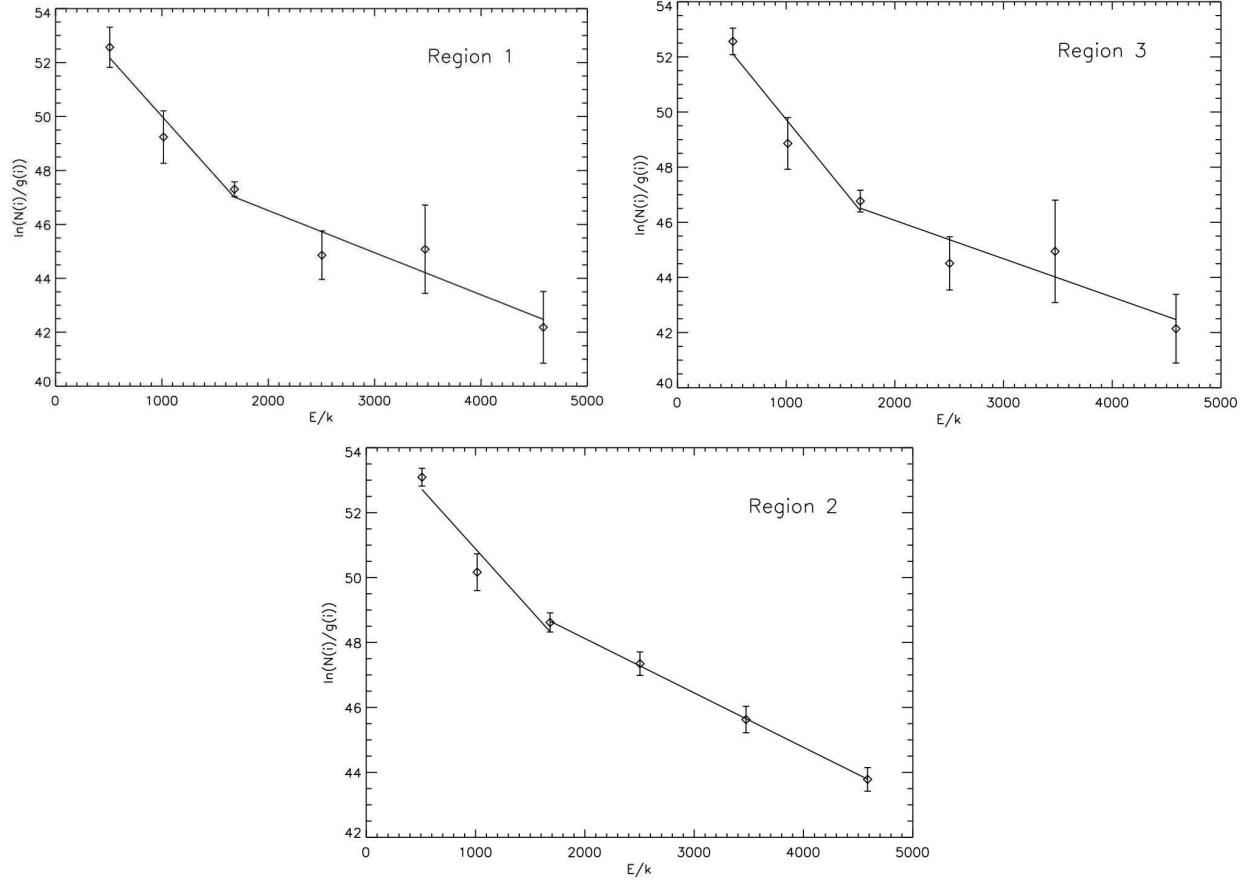


Fig. 4.— Shown are excitation diagrams and the fits to the warm and hot  $H_2$  phases taken from three different single pixel regions along the M51 strip. The different regions are marked on the  $H_2$  surface density maps in Figure 5.

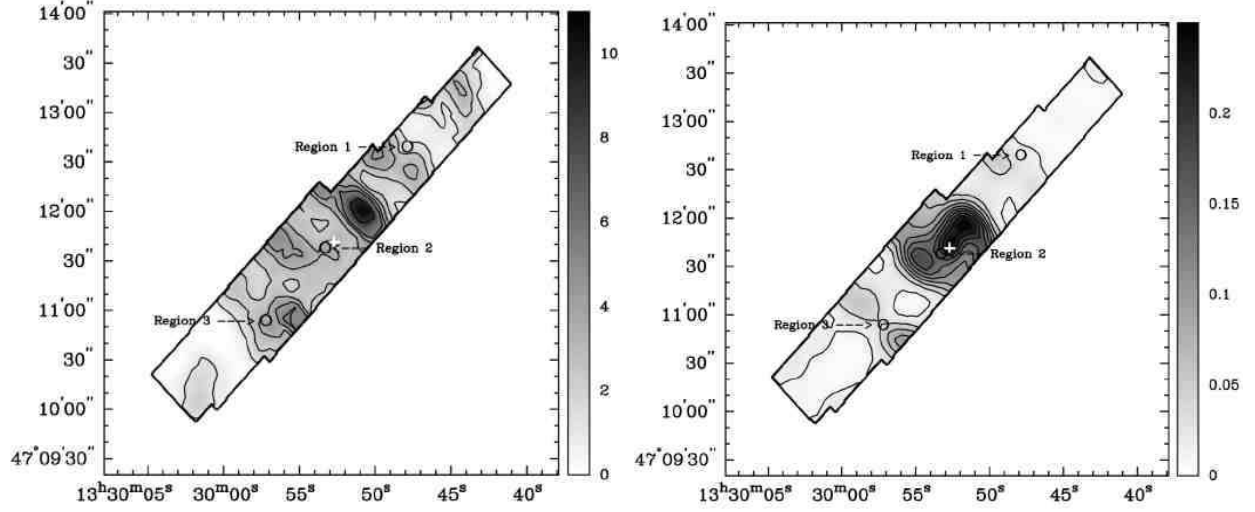


Fig. 5.— Shown are the warm ( $T = 100 - 300$  K)  $H_2$  (*left*) and hot ( $T = 400 - 1000$  K)  $H_2$  (*right*) surface density distributions. The surface density distributions are in units of  $M_\odot \text{ pc}^{-2}$ . Contours are overplotted for clarity. The warm  $H_2$  surface density contour levels are at 1.10, 2.21, 3.32, 4.43, 5.55, and  $8.85 M_\odot \text{ pc}^{-2}$ . The hot  $H_2$  contour levels are at intervals of 10 % of  $0.25 M_\odot \text{ pc}^{-2}$ . The hot  $H_2$  surface density distribution is derived from the fit to the  $H_2$  S(2) –  $H_2$  S(5) lines and the warm  $H_2$  surface density distribution is derived from the fit to the  $H_2$  S(0) –  $H_2$  S(2) lines, corrected for the contribution of the hot  $H_2$  phase. The three circles denote the regions of the spectra and excitation diagrams in Figures 2 and 4, respectively.

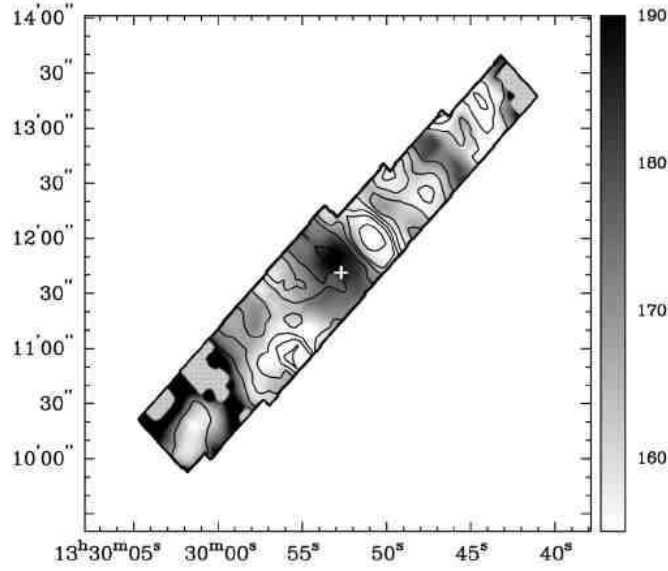


Fig. 6.— The warm ( $T = 100 - 300$  K)  $H_2$  surface density distribution (in contours) compared to the warm  $H_2$  temperature distribution (in grayscale, in units Kelvin). The warm  $H_2$  temperature and surface density distributions are derived from the fit to the excitation diagrams across the strip for the  $H_2$  S(0) –  $H_2$  S(2) lines, corrected for the contribution of the hot ( $T = 400 - 1000$  K)  $H_2$  phase. Surface density contour levels are at 1.10, 2.21, 3.32, 4.43, 5.55, and  $8.85 M_\odot \text{ pc}^{-2}$  (same as in Figure 5). The non-rectangular shape of the map is due to the slight offset of the *Spitzer* IRS SL strip relative to the LL strip. In both the northwest and southeast corners of the maps, the temperature and surface density distributions could not be determined due to no detection of the  $H_2$  S(0) line.

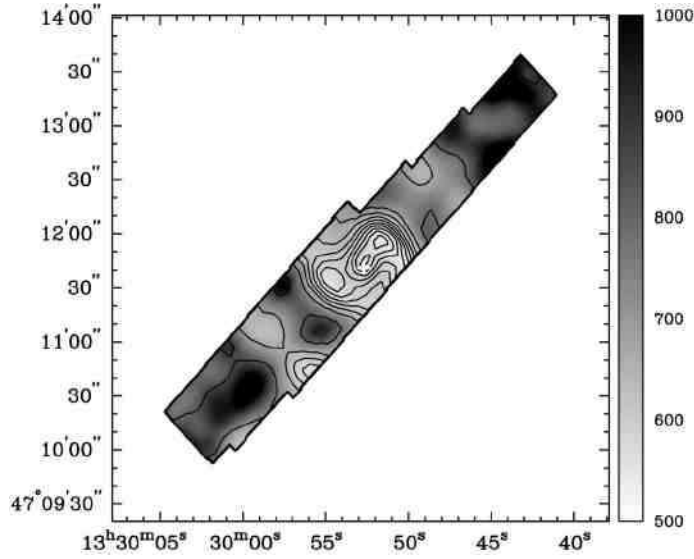


Fig. 7.— The hot ( $T = 400 - 1000$  K)  $H_2$  surface density distribution (in contours) compared to the hot  $H_2$  temperature distribution (in grayscale, in units Kelvin). The hot  $H_2$  temperature and surface density distributions are derived from the fit to the excitation diagrams across the strip for the  $H_2$  S(2) –  $H_2$  S(5) lines. Surface density contour levels are at intervals of 10% of  $0.25 M_\odot \text{ pc}^{-2}$  (same as in Figure 6). The high temperature and surface density of the hot phase towards the northwest and southeast ends of the strips is due to the lack of detection of extended emission from the  $H_2$  S(4) and  $H_2$  S(5) lines. In these regions (beyond the northwest and southeast spiral arms) we are unable to accurately determine the hot phase temperature and surface density.



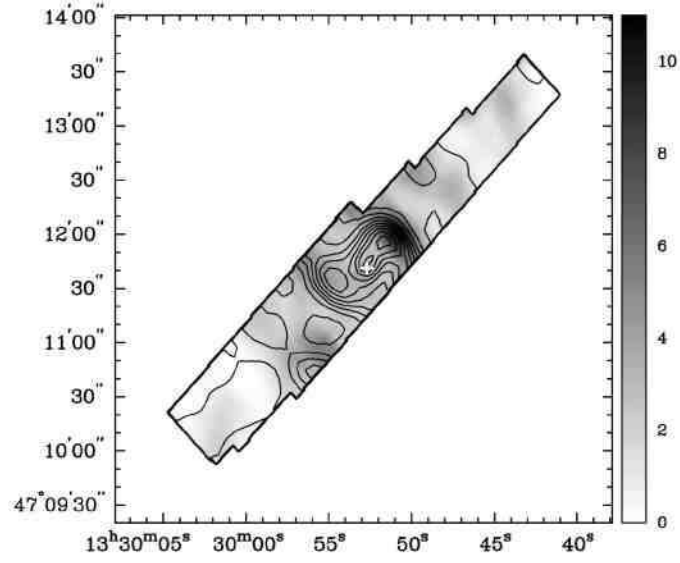


Fig. 8.— The warm ( $T = 100 - 300$  K)  $H_2$  surface density (in grayscale) compared to the hot ( $T = 400 - 1000$  K)  $H_2$  surface density (in contours). Contours levels for the hot  $H_2$  surface density distribution are at intervals of 10% of the maximum surface density ( $0.25 M_{\odot} \text{ pc}^{-2}$ ). The grayscale is in units of  $M_{\odot} \text{ pc}^{-2}$ .

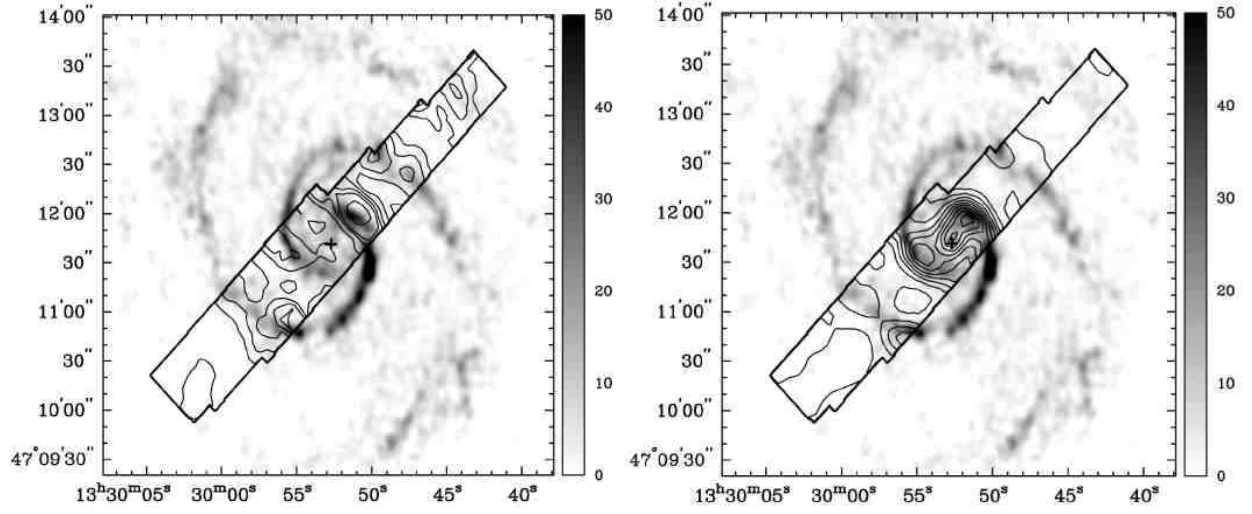


Fig. 9.— *Left*: Comparison of CO intensity (in grayscale) to the warm ( $T = 100 - 300$  K) H<sub>2</sub> surface density (in contours). The CO intensity is in units of Jy km s<sup>-1</sup>. The warm H<sub>2</sub> surface density contours are the same as in Figures 5 and 6. *Right*: Comparison of CO intensity (in grayscale) to the hot ( $T = 400 - 1000$  K) H<sub>2</sub> surface density (in contours). The CO intensity is in units of Jy km s<sup>-1</sup>. The hot H<sub>2</sub> surface density contours are the same as in Figures 5 and 7.

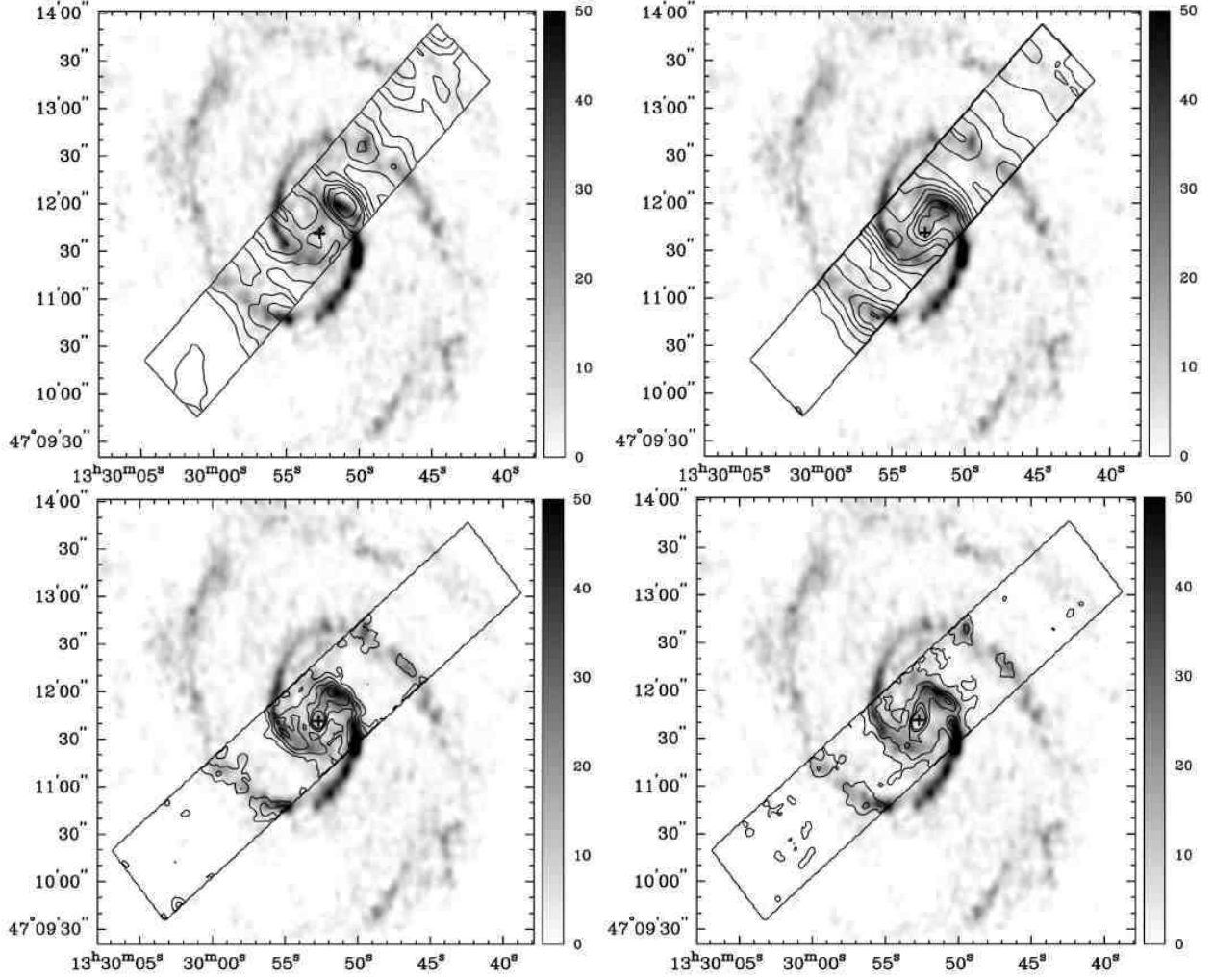


Fig. 10.— Comparison of the CO emission to the H<sub>2</sub> S(0) (*top left*), H<sub>2</sub> S(1) (*top right*), H<sub>2</sub> S(2) (*bottom left*), and H<sub>2</sub> S(3) (*bottom right*) emission. The CO emission maps are in units of Jy km s<sup>-1</sup>. Contour levels for H<sub>2</sub> S(0), H<sub>2</sub> S(1), H<sub>2</sub> S(2), and H<sub>2</sub> S(3) are the same as in Figure 3.

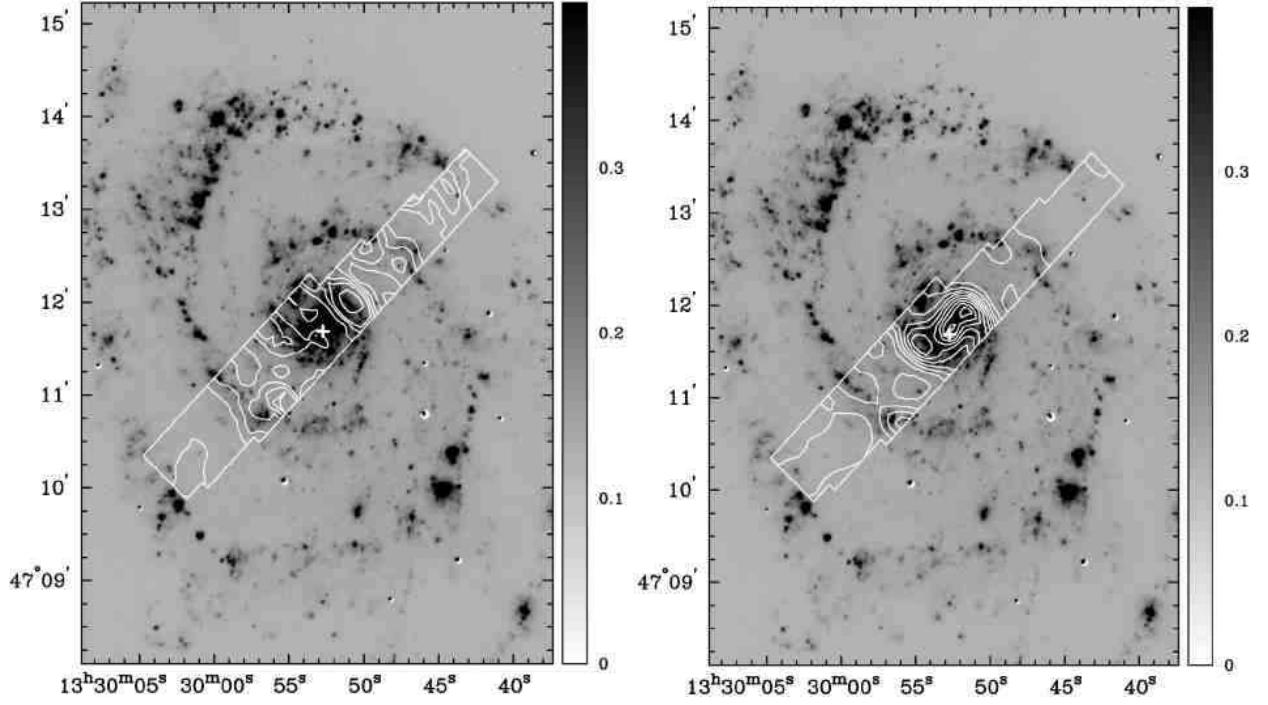


Fig. 11.— *Left*: Comparison of H $\alpha$  (in grayscale) to the warm ( $T = 100 - 300$  K) H $_2$  surface density (in contours). The H $\alpha$  image is in units of counts s $^{-1}$ . The warm H $_2$  surface density contours are the same as in Figures 5 and 6. *Right*: Comparison of H $\alpha$  (in grayscale) to the hot ( $T = 400 - 1000$  K) H $_2$  surface density (in contours). The H $\alpha$  image is in units of counts s $^{-1}$ . The hot H $_2$  surface density contours are the same as in Figures 5 and 7.

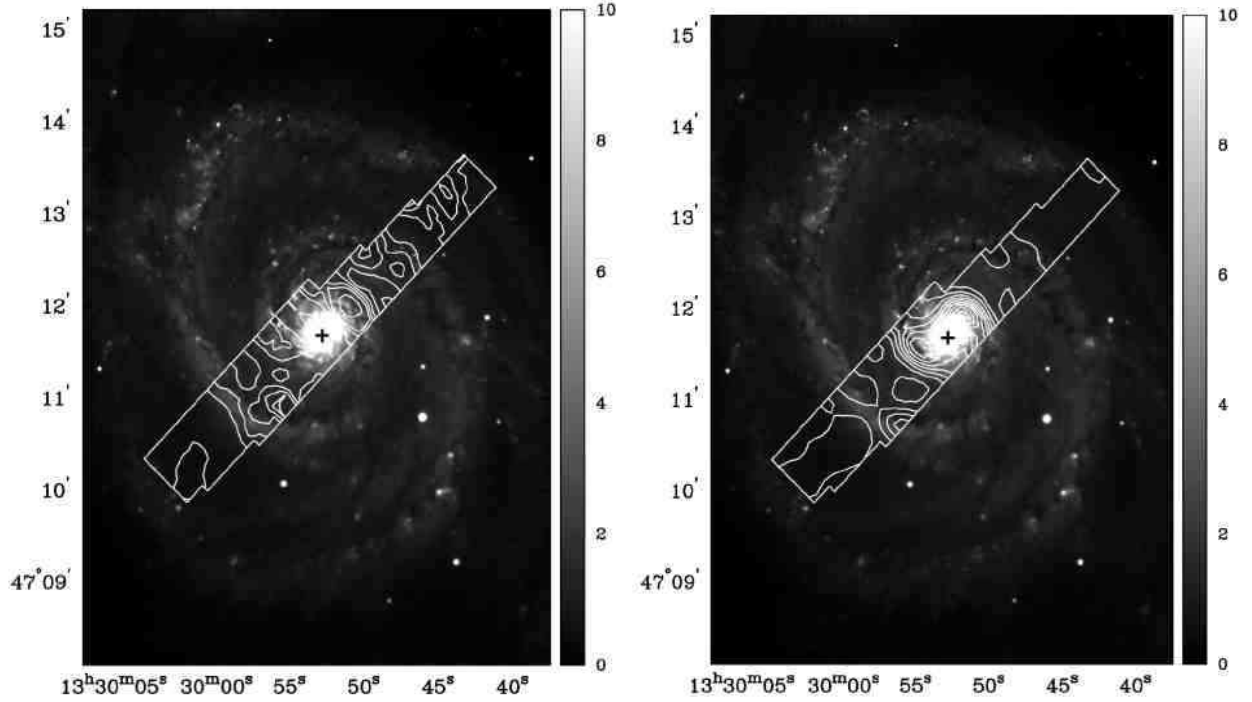


Fig. 12.— *Left*: Comparison of the  $V$  band image (in grayscale) to the warm ( $T = 100 - 300$  K)  $H_2$  surface density (in contours). The  $V$  band shows the dust lanes within M51. The  $V$  band image is in units of counts  $s^{-1}$ . The warm  $H_2$  surface density contours are the same as in Figures 5 and 6. *Right*: Comparison of  $V$  band image (in grayscale) to the hot ( $T = 400 - 1000$  K)  $H_2$  surface density (in contours). The  $V$  band image is in units of counts  $s^{-1}$ . The hot  $H_2$  surface density contours are the same as in Figures 5 and 7.

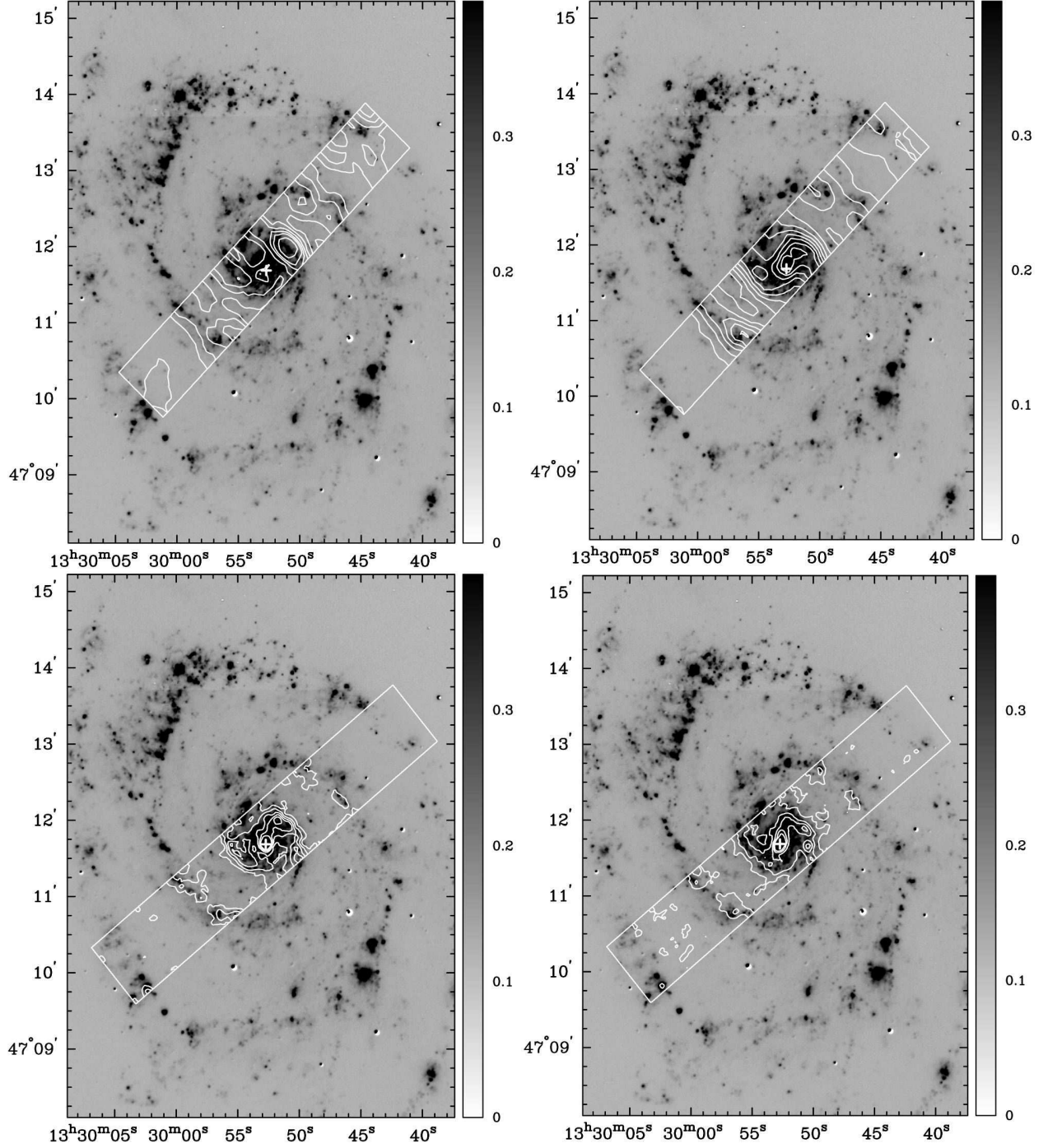


Fig. 13.— Comparison of H $\alpha$  emission to the H $_2$  S(0) (*top left*), H $_2$  S(1) (*top right*), H $_2$  S(2) (*bottom left*), and H $_2$  S(3) (*bottom right*) emission. The H $\alpha$  image is in units of counts s $^{-1}$ . Contour levels for H $_2$  S(0), H $_2$  S(1), H $_2$  S(2), and H $_2$  S(3) are the same as in Figure 3.

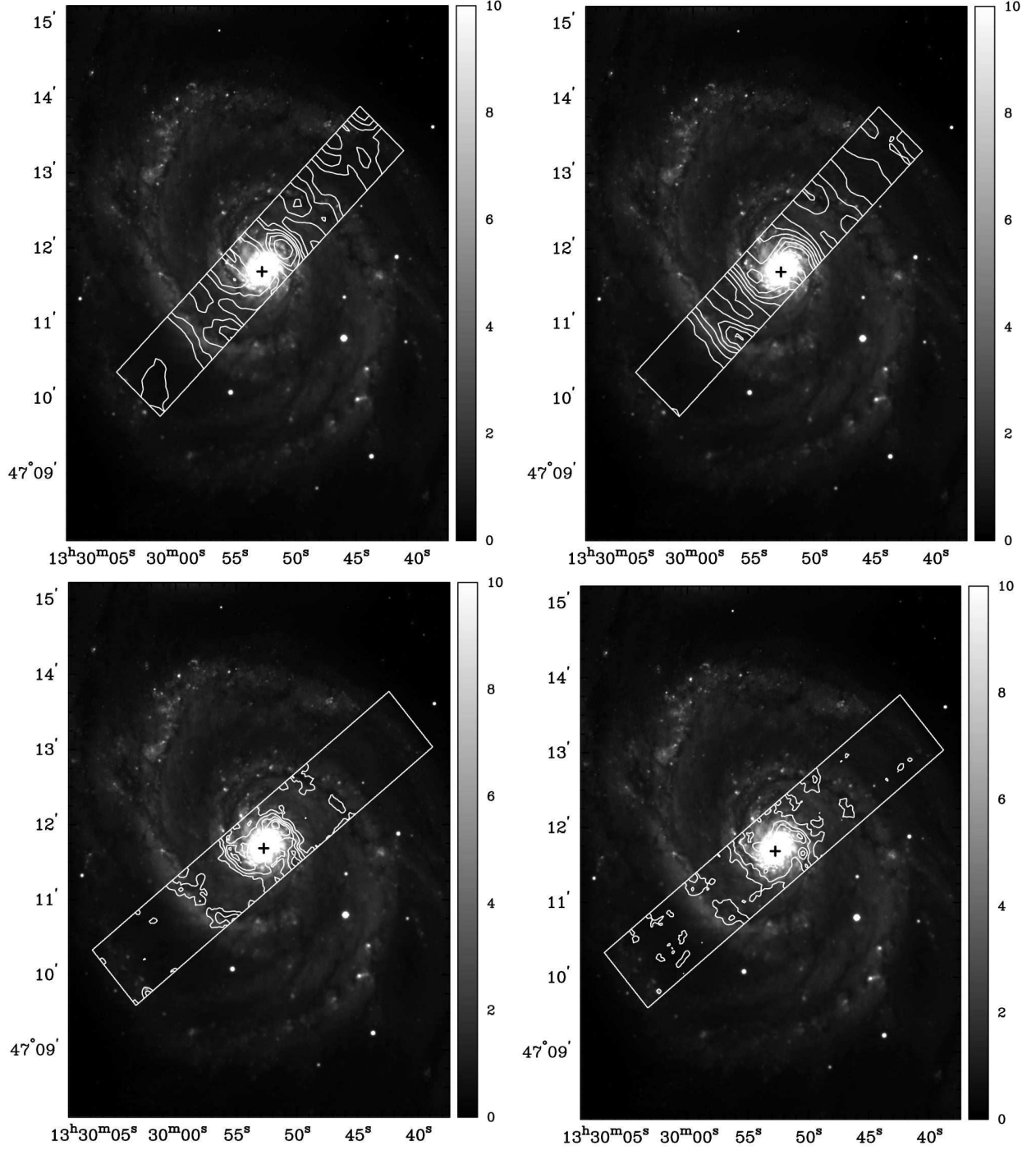


Fig. 14.— Comparison of the  $V$  band image to the  $\text{H}_2$  S(0) (*top left*),  $\text{H}_2$  S(1) (*top right*),  $\text{H}_2$  S(2) (*bottom left*), and  $\text{H}_2$  S(3) (*bottom right*) emission. The  $V$  band image is in units of counts  $\text{s}^{-1}$ . Contour levels for  $\text{H}_2$  S(0),  $\text{H}_2$  S(1),  $\text{H}_2$  S(2), and  $\text{H}_2$  S(3) are the same as in Figure 3.

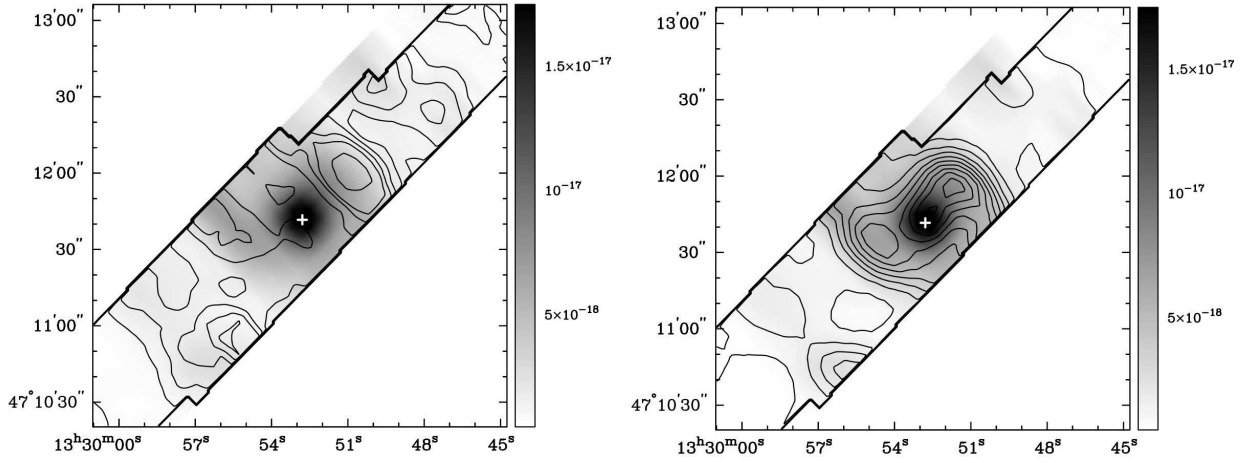


Fig. 15.— *Left*: Comparison of the [O IV](25.89  $\mu\text{m}$ ) emission (in grayscale) to the warm ( $T = 100 \text{ K} - 300 \text{ K}$ )  $\text{H}_2$  surface density distribution (in contours). Hot  $\text{H}_2$  surface density contours are the same as in Figures 5 and 6. *Right*: Comparison of the [O IV](25.89  $\mu\text{m}$ ) emission (in grayscale) to the hot ( $T = 400 - 1000 \text{ K}$ )  $\text{H}_2$  surface density distribution (in contours). Hot  $\text{H}_2$  surface density contours are the same as in Figures 5 and 7. The [O IV](25.89  $\mu\text{m}$ ) emission is in units of  $\text{W m}^{-2}$ .



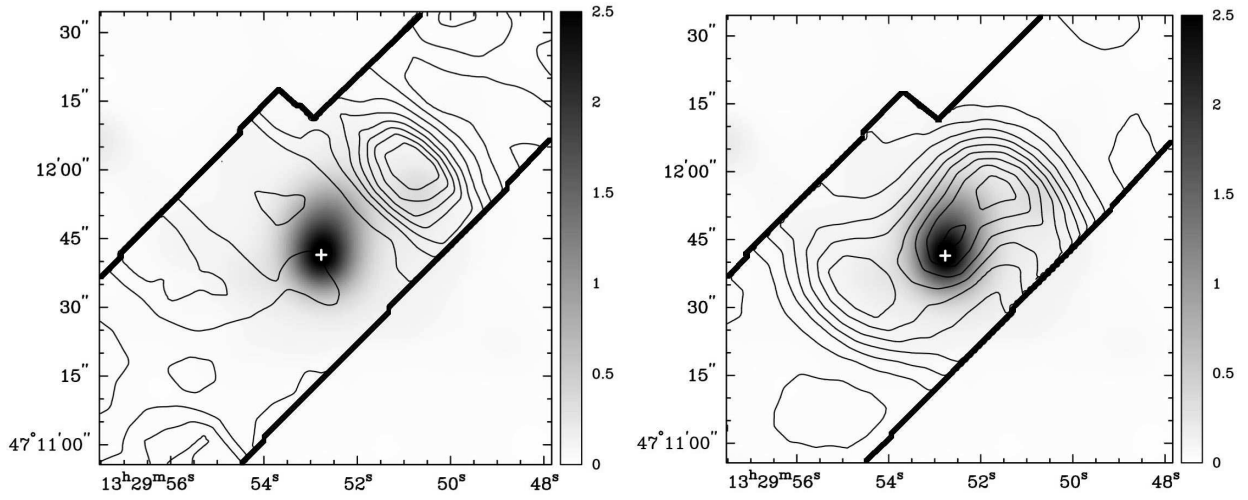


Fig. 16.— *Left*: Comparison of the smoothed 0.5 – 10 keV X-ray emission band (in grayscale) to the warm ( $T = 100 - 300$  K)  $H_2$  surface density distribution (in contours). The X-ray image has been smoothed to the same resolution as the warm  $H_2$  surface density map. X-ray emission is in units of counts. The warm  $H_2$  surface density contours are the same as in Figures 5 and 6. *Right*: Comparison of the smoothed 0.5 – 10 keV X-ray emission band (in grayscale) to the hot ( $T = 400 - 1000$  K)  $H_2$  surface density distribution (in contours). The hot  $H_2$  surface density distribution contours are the same as in Figures 5 and 7.

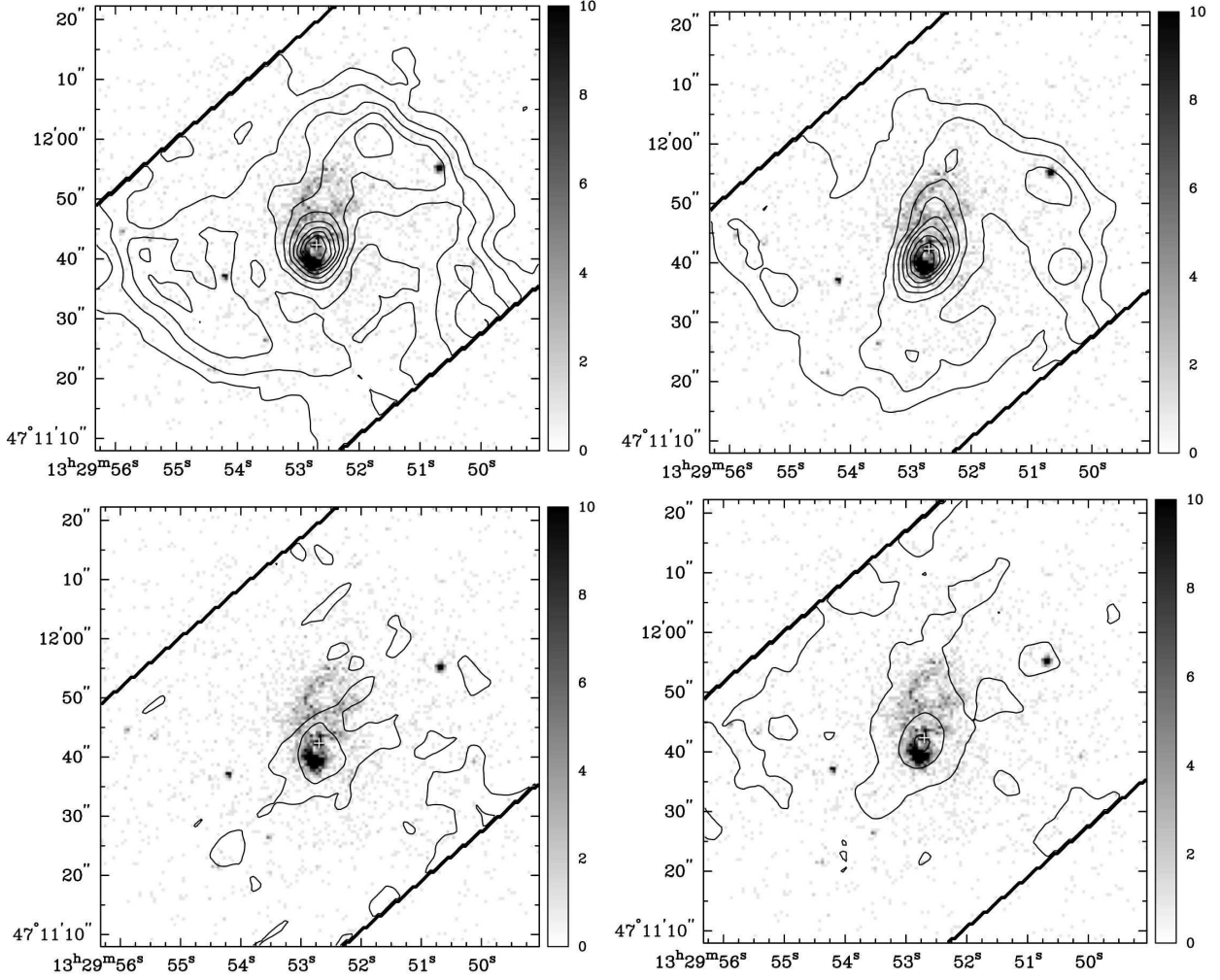


Fig. 17.— Comparison of the 0.5 – 10 keV X-ray emission band (in grayscale) to the H<sub>2</sub> S(2) (*top left*), H<sub>2</sub> S(3) (*top right*), H<sub>2</sub> S(4) (*bottom left*), and H<sub>2</sub> S(5) (*bottom right*) emission in the nuclear region of M51. X-ray emission is in units of counts. The H<sub>2</sub> S(2) and H<sub>2</sub> S(3) emission contours are at 10 % of their peak values ( $2.20 \times 10^{-18}$  and  $1.35 \times 10^{-17}$  W m<sup>-2</sup>, respectively). The H<sub>2</sub> S(4) contours are at  $1.0 \times 10^{-18}$  and  $2.0 \times 10^{-18}$  W m<sup>-2</sup> and the H<sub>2</sub> S(5) contours are at  $8.0 \times 10^{-19}$ ,  $4.0 \times 10^{-18}$ , and  $7.3 \times 10^{-18}$  W m<sup>-2</sup>.

Table 1. H<sub>2</sub> Parameters

Transition	Wavelength ( $\mu\text{m}$ )	Rotational State (J)	Energy (E/k)	A ( $\text{s}^{-1}$ )	Statistical Weight (g)
H <sub>2</sub> (0-0)S(0)	28.22	2	510	$2.94 \times 10^{-11}$	5
H <sub>2</sub> (0-0)S(1)	17.04	3	1015	$4.76 \times 10^{-10}$	21
H <sub>2</sub> (0-0)S(2)	12.28	4	1682	$2.76 \times 10^{-9}$	9
H <sub>2</sub> (0-0)S(3)	9.66	5	2504	$9.84 \times 10^{-9}$	33
H <sub>2</sub> (0-0)S(4)	8.03	6	3474	$2.64 \times 10^{-8}$	13
H <sub>2</sub> (0-0)S(5)	6.91	7	4586	$5.88 \times 10^{-8}$	45

Note. — The statistical weight (g) is  $(2J+1)(2I+1)$  where  $I$  equals 1 for odd J transitions (ortho transitions) and  $I$  equals 0 for even J transitions (para transitions).